OPEN

Resonant metamaterial detectors based on THz quantum-cascade structures

A. Benz[1], M. Krall[1], S. Schwarz[1], D. Dietze[1], H. Detz[2], A. M. Andrews[2], W. Schrenk[2], G. Strasser[2] & K. Unterrainer[1]

[1]Photonics Institute and Centre for Micro- and Nanostructures, Vienna University of Technology, Gusshausstrasse 29/387, A-1040 Vienna, Austria, [2]Institute of Solid-State Electronics and Centre for Micro- and Nanostructures, Vienna University of Technology, Floragasse 7/362, A-1040 Vienna, Austria.

We present the design, fabrication and characterisation of an intersubband detector employing a resonant metamaterial coupling structure. The semiconductor heterostructure relies on a conventional THz quantum-cascade laser design and is operated at zero bias for the detector operation. The same active region can be used to generate or detect light depending on the bias conditions and the vertical confinement. The metamaterial is processed directly into the top metal contact and is used to couple normal incidence radiation resonantly to the intersubband transitions. The device is capable of detecting light below and above the reststrahlenband of gallium-arsenide corresponding to the mid-infrared and THz spectral region.

Metamaterials are artificial structures consisting of individual sub-wavelength resonators where the electric and magnetic resonances are defined by the geometry of its constituents. Thereby, the electromagnetic permittivity and permeability can be engineered and decoupled from a bulk material response. This engineering control enables stunning optical properties that cannot be found otherwise in nature, such as superlensing[1,2], negative refraction[3,4] or cloaking[5]. Astonishingly, these properties can be realised with a single layer of sub-wavelength resonators, often referred to as a metasurface[6–8], making metamaterials very interesting for experiments as the fabrication remains fully compatible with conventional planar processing. This freedom in design and simplicity in fabrication enables the use of metamaterials in a variety of applications such as sensing[9], modulation of light[10] or beam control[6–8,11]. Furthermore, metamaterials allow for strong electric field enhancement in their vicinity[12] making them well suited to couple incoming light to a detector medium.

The optical properties of dipole transitions in semiconductor heterostructures can be engineered to a similar extent as the optical resonances in metamaterials using molecular growth techniques. Thin layers of different semiconductors form potential wells to confine carriers. The optical transitions are now restricted to quantized states with discrete energies. The energy and the dipole matrix element of these intersubband transitions (ISTs) can be controlled by the width of the individual barriers and wells leading to advanced concepts for light sources and detectors especially in the mid-infrared and terahertz (THz) spectral regions. Quantum-cascade lasers (QCLs) deliver tens of milliwatts over the entire wavelength range from 3 to 250 μm[13,14] except for wavelengths within the reststrahlenband of most III–V semiconductors ($\sim$25 to 35 μm). They are already used as sources for chemical detection in combination with standard detectors[15,16]. At the same time, quantum-well infrared photodetectors have shown to be excellent detectors in this frequency range[17–20], offering background limited infrared performance and high speed operation up to 110 GHz[21]. The next challenging step is merging the individual components into an integrated system monolithically to realize so-called lab-on-a-chip devices[22–24]. In principle, source and detector can be realized independently of each other and then packaged in close proximity. This approach seems feasibly for very small number of source-detector units but not for two-dimensional arrays. The main advantage of monolithic integration is the possibility to realize large arrays using conventional planar fabrication and omitting the need for any post-fabrication alignment steps.

Here, we present the design, fabrication and characterisation of a resonant detector based on a metasurface that couples light into an active THz quantum-cascade structure which operates below and above the reststrahlenband of gallium-arsenide (GaAs). The same heterostructure can be used to generate or detect light depending on the vertical confinement (double-metal waveguide[25] vs. metasurface) and the bias condition (forward bias vs. zero bias). A schematic of the detector is presented in Fig. 1. The key component is the metamaterial patterned directly into the metallic top contact. First, it provides the frequency selection for detection; only those frequencies of the incoming light that are resonant with the metamaterial can be measured. Second, most of the energy of the
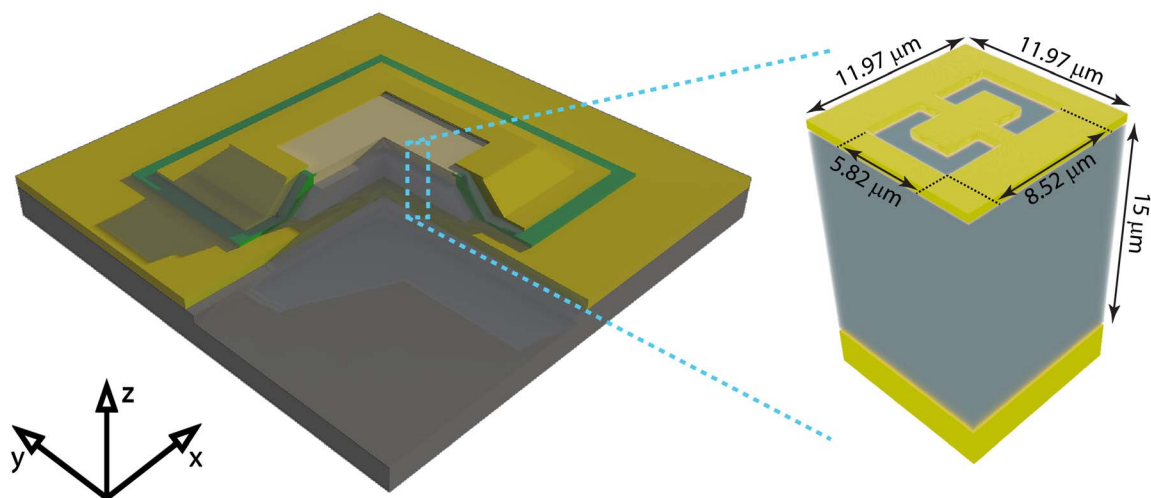
Figure 1 | Schematic metamaterial detector design. A double-metal waveguide confines the active region in the vertical direction. The metamaterial is patterned directly into the top contact, indicated by the dark yellow region. Extended contacts are processed onto the SiN$_x$ insulation shown in green. The coordinate system shows the direction of the fundamental axes used throughout this work. The inset shows the dimensions of one unit-cell and of the double-SRR. The width of the SRR traces and the gap between the two SRRs is 1.35 μm.

incoming light (propagating along the z direction) is transferred into the z component of the electric field (Ez) in the vicinity of the meta-material. This transfer is necessary as only the Ez field can interact with the ISTs due to the dipole selection rules. The efficient coupling of normal incidence light to ISTs via metamaterials has been demonstrated recently in the THz region[26–28]. It should be noted here that the responsivity of our detectors is expected to be low compared to state-of-the-art quantum-well infrared photodetectors[29–31] or quantum-cascade detectors[32–36]. Our active region is not optimized for detection efficiency but rather for integrating detectors and sources on the same chip using the same heterostructure. The fabrication process for our metamaterial detectors is compatible with the fabrication of conventional THz-QCLs in double-metal waveguides which allows us to build large arrays of sources and detectors that are realized at well-defined positions on the same chip. Since source and detector can be designed to operate at normal incidence, it becomes possible to analyse substances that are brought into proximity of the device surface. The emitted light at normal incidence hits the sample and is partly reflected towards the detector. Due to the possibility to tune the resonance frequencies of metamaterials and intersubband transitions we can potentially cover the MIR and THz spectral region.

Results

THz detection using a quantum-cascade laser active region. We first discuss the active region of our quantum-cascade detector which is based on a conventional THz-QCL. It consists of a GaAs/Al$_{.15}$Ga$_{.85}$As heterostructure grown by molecular beam epitaxy with the exact growth sequence: 8.0/**2.7**/6.6/**4.1**/15.5/**3.0**/9.2/**5.5** nm, where the bold letters represent the Al$_{.15}$Ga$_{.85}$As barriers and the normal letters the GaAs wells. The widest well is homogeneously doped to 8×10^{15} cm^{-3} while the rest of the cascade remains nominally undoped. The THz-QCL is based on the longitudinal optical (LO) phonon depopulation scheme[37] and is comparable to the structure described in Ref.[38]. It consists of 271 identical cascades resulting in a total thickness of 15 μm. If we process the active region into a conventional double-metal waveguide and apply forward bias, we can observe coherent light emission between 2.6 and 3.2 THz. The lasing threshold is around 650 A/cm^2 at 5 K, the maximum operating temperature in pulsed mode for the laser is 150 K. The basic experimental laser parameters at 5 K are summarized in Fig. 2a and Fig. 2b.

For the detector operation we use the same active region at zero bias, thereby minimising the dark current. A calculated bandstructure using an effective mass Schroedinger solver is presented in Fig. 2c. We include two cascades in our simulations (only one cascade is shown in Fig. 2c) and apply periodic boundary conditions. The ground state of the structure is located in the widest well. There are four main bound-to-bound transitions in this structure. The transition between states $|1\rangle$ and $|2\rangle$ (which we will call transition $|1\rangle$–$|2\rangle$ in the following for simplicity) has a transition energy of 16.8 meV (=4.1 THz) and goes to the miniband of states resulting in a broadened spectral response. The transition $|1\rangle$–$|3\rangle$ ends in the first excited state of the widest well and has a transition energy of 42.9 meV (=10.4 THz). The potential transition $|1\rangle$–$|3'\rangle$ has a transition energy of 35.9 meV (=8.7 THz) and will therefore be masked by the LO phonon in the experiment. The last bound-to-bound transition with a significant matrix element, occurring between states $|1\rangle$ and $|4\rangle$, has a transition energy of 88.9 meV (=21.5 THz). Due to its high eigenenergy and therefore weaker confinement, state $|4\rangle$ starts to span into the neighbouring cascades.

Photoresponse calculations. The interaction between an incoming light field and the quantum-well structure is modelled using the non-equilibrium Green's function (NEGF) method[39]. The main objective of the simulation is to study the active optical transitions and their contribution to the measured photocurrent. The studied heterostructure is homogeneous in the lateral direction while the current is flowing perpendicularly to the interfaces between two equilibrium reservoirs at both ends. The retarded and lesser Green's functions are given by,

$$G(E) = \left[(E - e\varphi)I - H_0 - \Sigma_S - \Sigma_D - \Sigma_{ph} \right]^{-1}$$
$$G^n = G \left(\Sigma_S^{in} + \Sigma_D^{in} + \Sigma_{ph}^{in} \right) G^+ \tag{1}$$

where E represents the energy, e the elementary charge, I the identity matrix, H_0 the Hamiltonian of the device, φ the electrostatic potential in the structure; Σ_D and Σ_S denote the self-energies accounting for the interaction with the contacts and Σ_{ph} the interaction with photons[40]. The Hamiltonian of the system is implemented in a real space basis using a single-band effective mass approximation[41]. The contacts are modelled as homogeneous leads simulating ohmic contacts[42]. A self-consistent solution of the Poisson equation for the electrostatic potential has not been
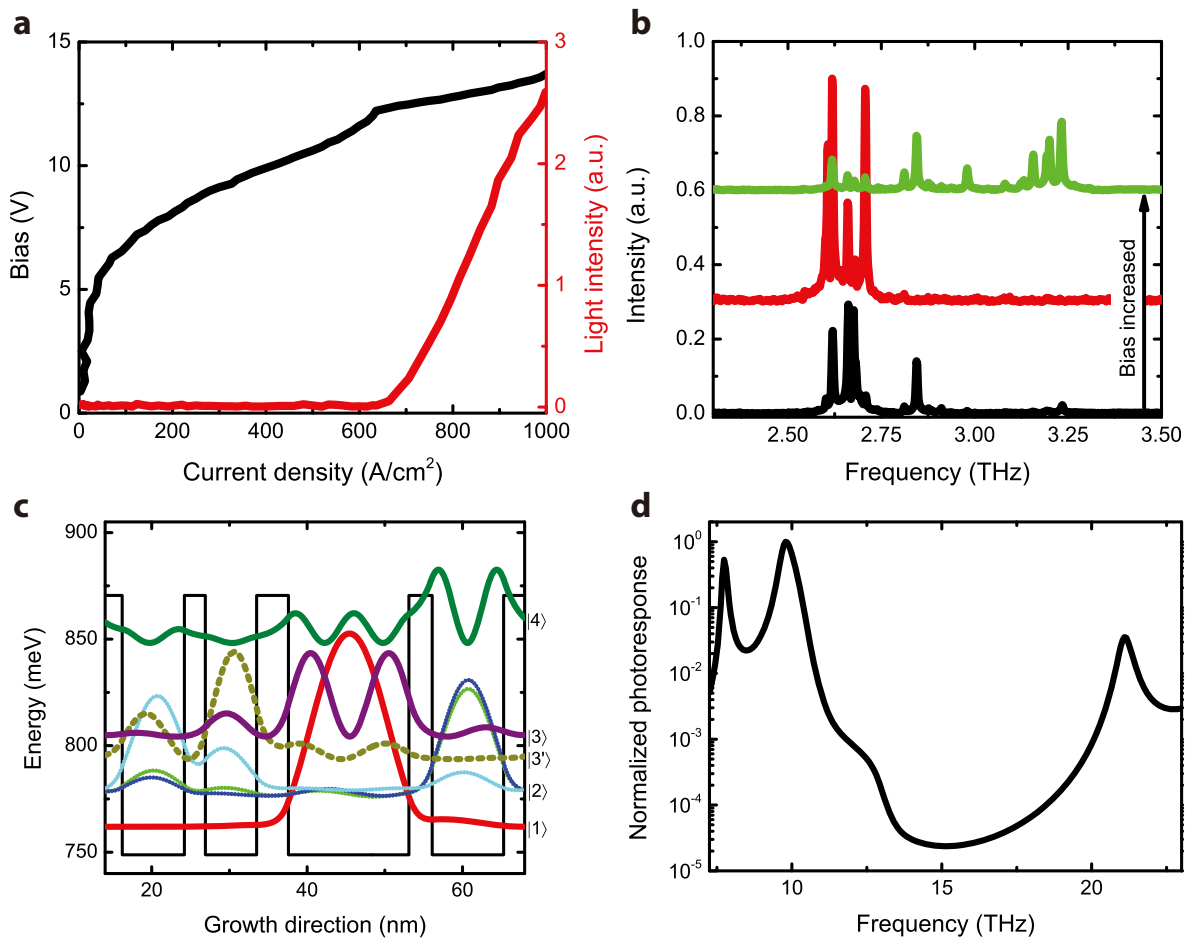
Figure 2 | Experimental laser characteristics and detector region simulations. (a), Experimental current-voltage and current-light characteristics at 5 K. The active THz quantum-cascade structure processed into a double-metal waveguide shows a lasing threshold of approximately 650 A/cm^2 under forward bias. (b), Experimental lasing spectra. For low bias voltage our lasers show emission between 2.6 and 2.8 THz. For higher bias voltage the lasing spectrum blue-shifts towards 3.25 THz. (c), Bandstructure at 0 kV/cm using an effective mass Schroedinger solver and assuming zero doping. The dominant states are marked with bold lines, the miniband $|2\rangle$ with dotted ones. The Fermi level energy is set to zero (y-axis). (d), Calculated photoresponse using NEGF simulations. The dominant transitions at 10 at the 21 THz are clearly visible. The predicted transition at 8.7 THz is masked by the LO phonon in the real device.

necessary due to the low doping concentration; the devices can be considered being in flat band condition.

In quantum-cascade lasers at low bias voltages (far below threshold), where LO phonon emission plays a minor role, electron transport is dominated by ballistic tunnelling[43]. Charge transport in the resonant metamaterial detector can also be assumed to be mainly determined by ballistic tunnelling as we operate the devices at zero bias. In order to calculate the photoresponse of the structure we include the effect of photon absorption on electron transport in the device. The full non-local electron-photon interaction is included in the self-consistent Born approximation. We assume that absorption processes dominate and therefore neglect emission terms[40]. The photoresponse calculations are performed in the linear regime. A detailed discussion on the NEGF calculations can be found in Ref.[44].

The calculated photoresponse for frequencies above the reststrahlenband is presented in Fig. 2d. We can clearly identify two peaks at frequencies that correspond to the transitions $|1\rangle$–$|3\rangle$ and $|1\rangle$–$|4\rangle$ in our bandstructure calculation (Fig. 2c). The third peak around 8 THz corresponding to the $|1\rangle$–$|3'\rangle$ transition appears strong in the simulations but is masked in the measurements by the LO phonon absorption. It should be noted here that the optical phonon itself does not lead to any photoresponse of the device which allows us to remove its effect from the NEGF calculations and thereby simplify them. The photoresponse of the structure is calculated in a short

circuit configuration (zero external bias). The resulting current is caused by the asymmetry of the electronic wavefunctions that act like a built-in electric field and move the carriers preferentially into one direction. This is a typical behaviour for quantum-cascade detectors operated as photovoltaic devices.

Resonant metamaterial design. The metamaterial used throughout this work is based on a complementary double split-ring resonator (SRR) which is arranged in a periodic two-dimensional array. In general, a conventional metamaterial consists of an array of subwavelength metallic resonators processed on top of a dielectric substrate. Their reflection and transmission characteristics depend on the exact size and shape of the metallic resonators. Complementary metamaterials on the other hand consist of a thin metallic sheet covering the entire substrate with an array of subwavelength holes. Again, the reflectance and transmittance depend on the size and shape of these holes. This inverted geometry also leads to inverted frequency behaviour. According to Babinet's principle the reflectance and transmittance coefficients of a conventional metamaterial and its complementary counterpart have to be swapped[45]. In other words, a transmittance minimum for the conventional metamaterial translates to a reflectance minimum for the complementary metamaterial. For the final device the complementary metamaterial offers two main advantages. First,

the top layer forms the top electrical contact naturally without introducing any additional metal stripes connecting the individual SRRs and acting as bias lines. Second, it forms an almost perfect double-metal waveguide together with the metallic ground plane used as the bottom contact. The waveguide is essential to ensure a high overlap between the active detector region and the mode coupled by the metamaterial for the lowest intersubband transition at 4.1 THz (equivalent to a free space wavelength of 73 μm). For the two higher frequency transitions (10.4 and 21.5 THz) the double-metal waveguide does not provide any significant confinements as those modes are located close to the metamaterial surface.

Before we can analyse the full detector response, it is necessary to understand the interaction between metamaterial resonances and ISTs in general. The detector can only produce an electrical signal when we are able to couple light to the IST. Incident light that does not overlap in energy with the IST cannot excite an electronic transition and therefore create any electrical signal. This means that we can restrict our analysis to three main frequency regions: 4.1, 10.4 and 21.5 THz which correspond to the three dominant transitions of our heterostructure. Another essential aspect for the detector operation that has not been discussed in detail so far is the polarization selection rule for an IST in a GaAs based heterostructure. As mentioned earlier, QWs lead to a quantization of the electronic wavefunctions only along one direction (in this manuscript labelled as the z-axis). This layered structure results in an anisotropic dielectric permittivity; only the electric field component that is polarized along the growth direction (here labelled as z-axis) can interact with the ISTs. Since we are analysing normal incidence radiation (propagating along the z-axis) we expect no response from our heterostructure on its own. We have to provide the z-component for the electric field by some other mechanism. The metamaterial on top of our detector region has the important role to transfer energy efficiently from the incoming light into the z-component in its vicinity. Therefore, the expected detector response is a convolution of the available ISTs in our heterostructure (other frequencies cannot create any electrical signal) and the Ez components of the electric field created by our metamaterial (the other electric field polarizations cannot couple to the ISTs).

To design our metamaterial and its resonances we use finite-difference time-domain (FDTD) simulations[46]. We model one period according to the dimensions shown in the inset of Fig. 1 and apply periodic boundary conditions. We use a square unit-cell with a side length of 11.97 μm along the x and the y axes. The height of the QW-region is set to 15 μm, corresponding to the thickness of our grown heterostructure. The top metal contact has a thickness of 500 nm while the bottom gold layer is set to 2 μm. In our calculations we model both gold layers as perfect metals which simplifies the calculation without reducing the accuracy significantly. We can make this simplification as our devices are operating around the reststrahlenband (10 THz) while the plasma frequency of gold is at 2175 THz[47]. We have added simulation results comparing the predicted metamaterial resonances obtained for a perfect metal with realistic values for gold to the Methods Section to confirm our assumption.

The permittivity of the active heterostructure is modelled in two steps. First, we approximate the complex permittivity of the GaAs/Al$_{.15}$Ga$_{.85}$As quantum-cascade structure by using the relative fraction of GaAs versus AlAs and calculating a weighted average (details are given in the Methods section). The parameters for the two binaries GaAs and AlAs around the reststrahlenband are taken from literature[48]. This procedure gives us the isotropic, frequency-dependent, background of our device. In a second step we add the effect of the three main IST which are modelled as three anisotropic harmonic oscillators following the dipole selection rules for ISTs with their centre frequencies of 4.1, 10.4 and 21.5 THz. We experimentally verified the transition energies of the two higher frequency transitions by intersubband absorption measurements using an unprocessed

piece from the same wafer. Details on the modelling of the semiconductor and on the absorption measurements are given in the Methods section.

The main reason to choose the double-SRR for this work is the large number of higher order resonances. This allows us to couple a wide range of incoming frequencies to the underlying ISTs using the same metamaterial film. Simulated field profiles for excitations at the three fundamental intersubband resonances are presented in Fig. 3a. The simulations show the z-component of the absolute value of electric field (the component coupling to ISTs) 500 nm underneath the top metal contact. Depending if the incoming light is polarized along the x or y-axis, we can excite different modes of the metamaterial. The different spatial mode profiles for the x and y polarized excitation already indicate that our device response goes beyond a simple grating coupler which would have the same frequency response for both polarizations (we use a square unit cell).

To verify the existence of metamaterial resonances and separate them from a pure grating response, we perform simulations where the double-SRR size is kept constant (we use the same double-SRR dimensions as shown in the inset in Fig. 1) while the period is changed from 11.97 (original) to 8.98 (minus 25%) and 14.96 μm (plus 25%). Ideally, a pure grating response will depend only on the period of the unit-cell while a pure metamaterial response will be independent. We show the calculated metamaterial resonances around the dominant IST (10.4 THz) for incoming light polarized along the x and y-axis in Fig. 3b and Fig. 3c respectively. The results for Ex incoming light show three resonances that are almost independent of the unit-cell size (or period) at 9.24, 9.67 and 10.51 THz and can therefore be attributed to the metamaterial. However, if we rotate the excitation polarization to the Ey direction, strong grating modes appear that show the expected shift with periodicity from 10.27 THz (8.98 μm period) to 9.55 THz (14.96 μm period). It should also be noted that the amplitude of the resonances differs greatly depending on the excitation polarization confirming that our devices operate on higher order metamaterial resonances rather than simple grating modes. The complex mixture of grating and metamaterial resonances is expected as the metamaterial has a periodicity that is comparable to the effective wavelength inside the semiconductor.

Another aspect that has to be considered is the thickness of the waveguide which is also comparable to effective wavelength inside the semiconductor. Therefore, we can expect the electric field to vary along the depth. In Fig. 3d we present three cuts in the xy-plane (parallel to the metamaterial layer) at different depths for an excitation at 42.9 meV (10.4 THz). The Ez-field is strongest just underneath the top metal and close to the bottom metal contact; it is weakest in the centre of the waveguide. Therefore, the electric signal that we measure will be limited by the low absorption in the centre of the waveguide.

Device fabrication. The processing of the metamaterial-based detectors follows the recipes of standard THz-QCLs in double-metal waveguides[25]. After a thermo-compression bonding of the epitaxial layer to a doped receptor substrate, the original substrate is removed by lapping and selective wet chemical etching. The metamaterial layer is defined by optical lithography. A scanning electron microscope image of one meta-atom is presented in Fig. 4a. In the next step, the mesas are etched isotropically using wet chemical etching. The additional mesa definition suppresses unwanted leakage currents while the wedged sidewalls simplify the SiN$_x$ insulation. The top contact is processed onto an extended contact pad to allow for wire bonding. Thereby, we ensure that the bonding wire does not interfere with the metamaterial mode[49]. The metamaterial openings are etched 500 nm into the semiconductor which removes the highly doped n$^+$-layer and prevents the shorting of our metamaterial. In a last, step the entire sample is annealed to
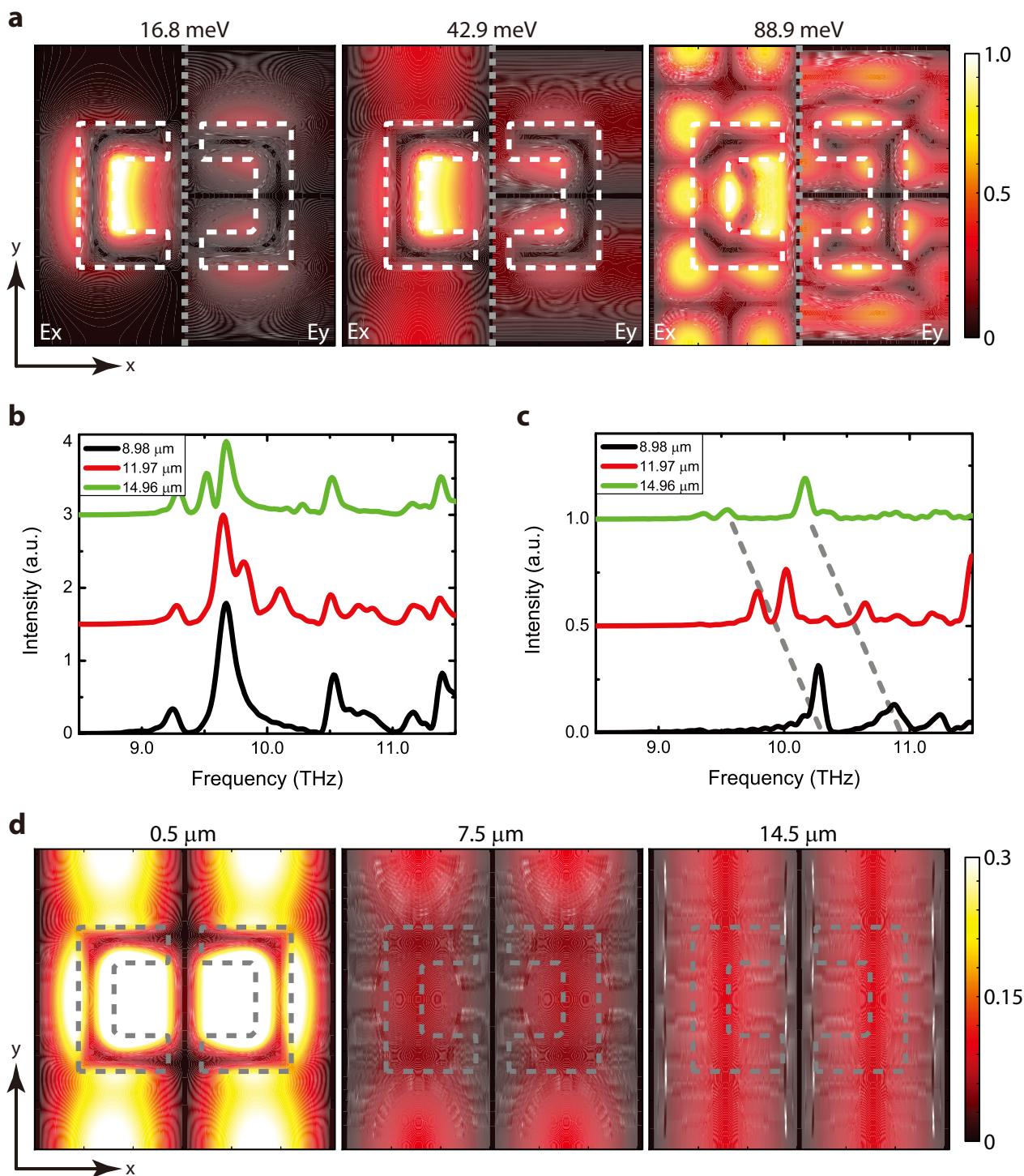
Figure 3 | Simulated electric field distributions and cavity resonances. (a), The contour plots show the absolute value of the integrated E_z component 500 nm below the top metallic contact inside the semiconductor for a device with a period of 11.97 μm and excitations at 16.8, 42.9 and 88.9 meV (from left to right). The left (right) panel for each excitation energy shows the field for an incident polarization along the x (y) axis. The dashed white line shows the position of the SRR. (b, c), Metamaterial resonances calculated for a fixed double-SRR size but varying periods. The system is excited with a plane wave polarized either along the x-axis (shown in panel (b)) or the y-axis (shown in panel (c)). The spectra are calculated for periods of 11.97 (original value), 8.98 (minus 25%) and 14.96 (plus 25%). The excitation pulse is identical in amplitude and spectrum for both cases; we only rotate the polarization to obtain the two results. The individual curves are offset vertically for clarity. The grey dashed lines in panel (c) are a guide to the eye demonstrating the shift of the grating mode. (d), The E_z component for a metamaterial with a period of 11.97 μm and an excitation at 42.9 meV polarized along the x-axis. The different contour plots (from left to right) show the simulated field 0.5 μm, 7.5 μm (in the middle of the active region) and 14.5 μm (just above the bottom contact) below the top contact.
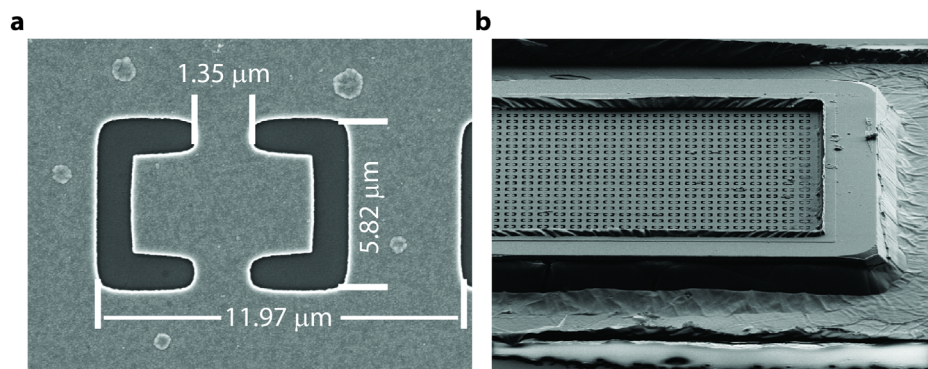
Figure 4 | Scanning electron microscopy images of the metamaterial. (a), The dimensions given in the scanning electron micrograph image correspond to the a metamaterial period of 11.97 μm. (b), The active area is structured into a mesa to suppress leakage currents. The extended contact pads prevent any influence of the bonding wire onto the metamaterial mode.

achieve ohmic contacts. A scanning electron microscopy image of a final device is shown in Fig. 4b. The fabrication is described in more detail in the Methods section.

Experimental results. Besides the metamaterial device discussed in the Resonant Metamaterial Design section (period 11.97 μm), we have fabricated metamaterials with three additional periods (8.54, 9.15 and 10.56 μm). For the different devices we have scaled the period and the size of the double-SRR at the same time using the same geometric scaling factor. In other words, the geometric size relationship between double-SRR and period remains constant for all our devices. This geometric scaling of the metamaterial allows us to control its resonance frequencies and tune them across the fixed ISTs (we are always using the same semiconductor wafer for all devices). Thereby, we can study the coupling as a function of the metamaterial and IST resonances. All the devices are mounted onto a copper heat-sink, placed inside a liquid-Helium cryostat and cooled to 5 K. For the spectral characterisation we use a Bruker Vertex80 where the light from a globar is directed through the interferometer and then focused onto the detector under normal incidence. The metamaterial is used to couple the incoming light to the IST resulting in an expected photoresponse that is a convolution of the ISTs and the metamaterial resonances. The FDTD simulations indicate metamaterial modes however no intersubband transitions are present. Therefore, none of the samples shows any response between 6 and 9 THz or between 11 and 17 THz.

We focus our experimental analysis to the frequency region around the dominant IST (10.4 THz) and start with the polarization dependence of a metamaterial detector with the period of 9.15 μm (Fig. 5a). As already predicted by our simulations, we expect the detector response to show a clear difference between Ex and Ey excitation. For an Ex polarization we see a sharp resonance around 10.14 THz. The detector response under Ey excitation is significantly weaker, missing this sharp feature while showing its only clear maximum at 10.25 THz. The numeric addition of the detector responses for both incoming polarizations precisely recovers the detector response for an unpolarized excitation which can be expected from a linear system.

The comparison between the experimental detector response and the calculated metamaterial resonances using FDTD simulations for all four metamaterial periods and Ex polarized excitation is presented in Fig. 5b. The detector with a period of 8.54 μm shows one dominant peak around 10.16 THz and a weaker one at 9.2 THz in the experiment. Both peaks agree well with the predicted metamaterial resonances for this period. An increase of the metamaterial period to 9.15 and 10.56 μm leads to the expected redshift of the dominant peak to 10.14 and 9.95 THz in the experiment. A similar resonance shift towards lower frequencies is also observable in the calculated

metamaterial responses. It should be noted that not only the position of the resonances agrees well between simulation and experiment but also their lineshapes. The smaller periods (8.54 and 9.15 μm) show a slow increase for frequencies below and a sharp drop for frequencies above the resonance. The device with a period of 10.56 μm shows a more symmetric lineshape for the dominant metamaterial resonance. The 11.97 μm device shows a broad background response with one very sharp feature at 10.25 THz. The broad background can be expected as the metamaterial resonance and the IST overlap well in energy. The narrow feature agrees reasonable with a metamaterial resonance around 10.1 but not with the predicted amplitude. In the experiment, it appears much stronger than our simulations predict. The discrepancy between theoretical and experimental resonance frequencies for all four metamaterial detectors is attributed partly to the uncertainty in refractive index of the semiconductor. The values we use in our model for the GaAs/Al$_{.15}$Ga$_{.85}$As heterostructure are obtained from room temperature measurement; however our detector measurements are performed at 5 K.

The low and high frequency response of a detector with a period of 11.97 μm is presented in Fig. 5c. The photoresponse corresponding to the $|1\rangle$–$|2\rangle$ transition is clearly visible. The observed broad spectrum is expected as the transition ends in a miniband of states. The detector response around 18 THz is caused by transitions between higher lying states inside the heterostructure. We attribute that to a higher carrier concentration at the top and the bottom of our 15 μm thick quantum-well stack. In order to ensure low resistance electrical contacts we added thin, highly doped n$^+$-layers (50 nm, 5 × 10^{18} cm^{-3}) to our sample growth which increases the electron concentration in the adjacent quantum-wells and populates state $|2\rangle$ even at 5 K. The transition $|1\rangle$–$|4\rangle$ appears around 20 THz as expected. However, it cannot be captured fully in the experiment due to the limited bandwidth of our beamsplitter.

Discussion

We have demonstrated a metamaterial detector utilising an active THz quantum-cascade structure which is capable of normal incidence operation. The metamaterial rotates the polarization of the incoming radiation in the near-field and makes it compatible with the dipole selection rules present in semiconductor quantum-wells. Light is only detected if the metamaterial mode overlaps energetically with quantum-well transitions (the spatial overlap is ensured by the double-metal waveguide). The presented devices use double-SRRs with large numbers of modes; light can be coupled to all three bound-to-bound transitions (4.1, 10.4 and 21.5 THz) in the quantum-well region using the same metamaterial. All experimental detector curves show very distinct peaks that are in good agreement with the calculated metamaterial resonances. As demonstrated in the
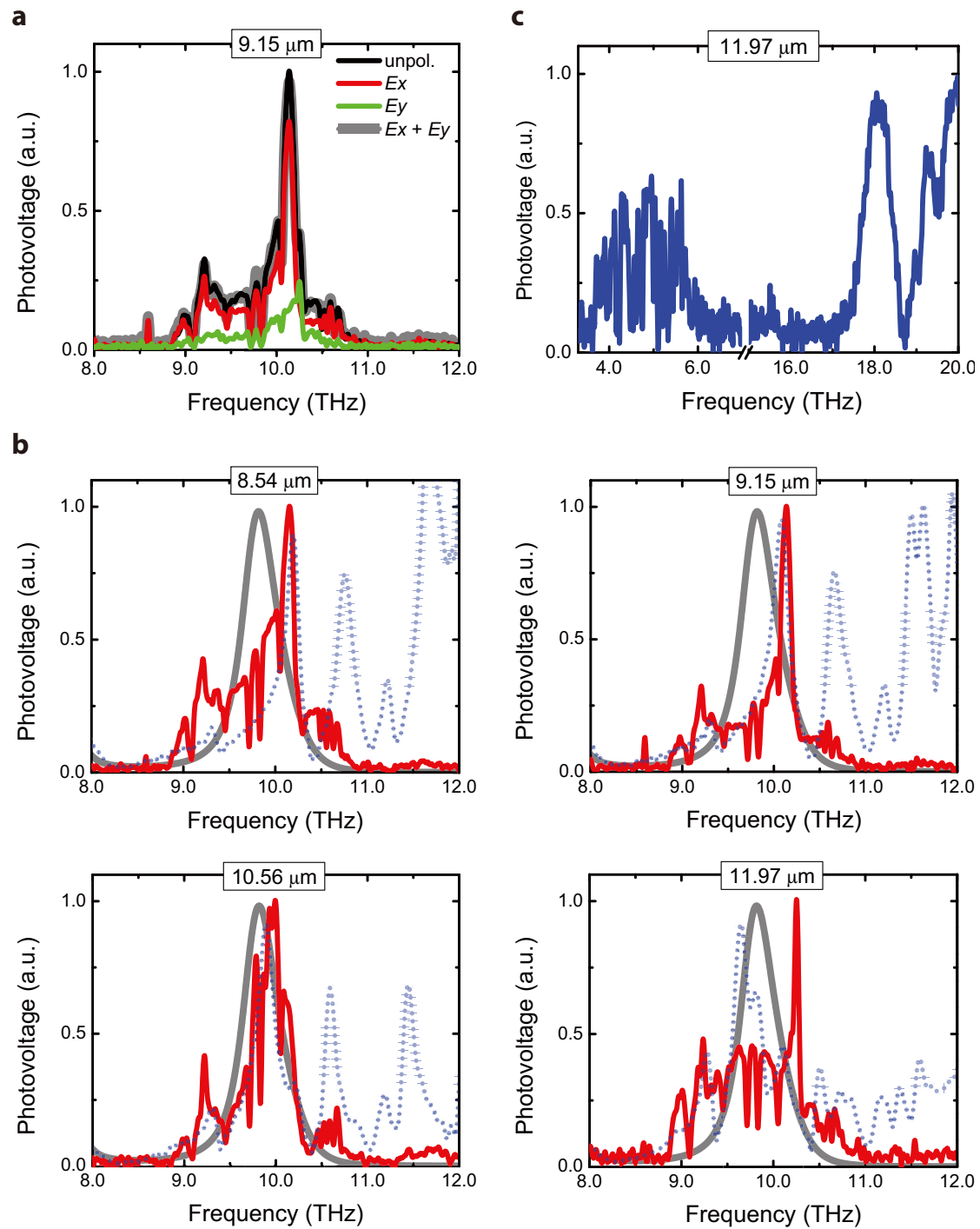
Figure 5 | Comparison of measured detector spectra and calculated metamaterial resonances. (a), Detailed measurements for a detector with a period of 9.15 μm. The addition of the detector response (grey) for *Ex* (red) and *Ey* (green) excitations recovers exactly the experimental unpolarized response (black). The unpolarized response is multiplied by 0.67 to compensate for the reflection at the ZnSe polarizer. (b), Measured photovoltage spectra for a metamaterial detectors with period of 8.54, 9.15, 10.56 and 11.97 μm under *Ex* excitation. The predicted metamaterial resonances represented by the dotted, blue lines are calculated using FDTD simulations. We analyse only the *Ez* component in the vicinity of the top metal contact as this is the only polarization component that can couple to the intersubband transitions. The grey line represents the calculated lineshape of the intersubband transition using NEGF calculations. (c), Experimental spectra for a period of 11.97 μm showing the unpolarized response at low and high frequencies. The predicted transition $|1\rangle$–$|2\rangle$ appears very broad as it ends in a miniband of states. This period shows the strongest photovoltage response at frequencies in the range of 18 to 20 THz.

experiments, the detector response goes beyond a simple grating coupler. If the system could be described as a simple two-dimensional Bragg grating, the photoresponse would be identical for both polarizations as we use a square unit-cell. To understand the operation of

our detector it is necessary to perform a careful simulation including the excitation polarization, the size of the double-SRR and the periodicity. All three parameters determine the detector response to incoming light.

Table 1 | Material parameters used for GaAs and AlAs around the reststrahlenband frequency region[48]

	GaAs	AlAs
ε_∞	11.0	8.16
ω_{LO} (cm^{-1})	292.1	400.6
ω_{TO} (cm^{-1})	268.7	359
γ (cm^{-1})	2.4	3.2

Methods

Material parameters for the finite-difference time-domain simulations. The effective permittivity for the quantum-well region including the effect of the ISTs is modelled in two steps. First, we describe the background permittivity of the GaAs/Al$_{.15}$Ga$_{.85}$As heterostructure using literature values for GaAs and AlAs around the reststrahlenband[48].

$$\varepsilon_{back}(\omega) = w_{GaAs}\varepsilon_{\infty,GaAs}\left(1+\frac{\omega^2_{LO,GaAs}-\omega^2_{TO,GaAs}}{\omega^2_{TO,GaAs}-\omega^2-i\omega\gamma_{GaAs}}\right)$$
$$+ w_{AlAs}\varepsilon_{\infty,AlAs}\left(1+\frac{\omega^2_{LO,AlAs}-\omega^2_{TO,AlAs}}{\omega^2_{TO,AlAs}-\omega^2-i\omega\gamma_{AlAs}}\right), \qquad (2)$$

where w_{GaAs} and w_{AlAs} are the relative weights of pure GaAs and AlAs found in the GaAs/Al$_{.15}$Ga$_{.85}$As heterostructure. The other parameters describe the dispersion of GaAs and AlAs respectively around the reststrahlenband and are listed in Table 1. Using the exact growth sequence for our heterostructure which is 8.0/**2.7**/6.6/**4.1**/15.5/**3.0**/9.2/**5.5** nm (bold letters represent the Al$_{.15}$Ga$_{.85}$As barriers), we can calculate the relative weights to be: w_{GaAs} = 95.8% and w_{AlAs} = 4.2%. The background permittivity for our THz quantum-cascade structure is presented in Fig. 6a.
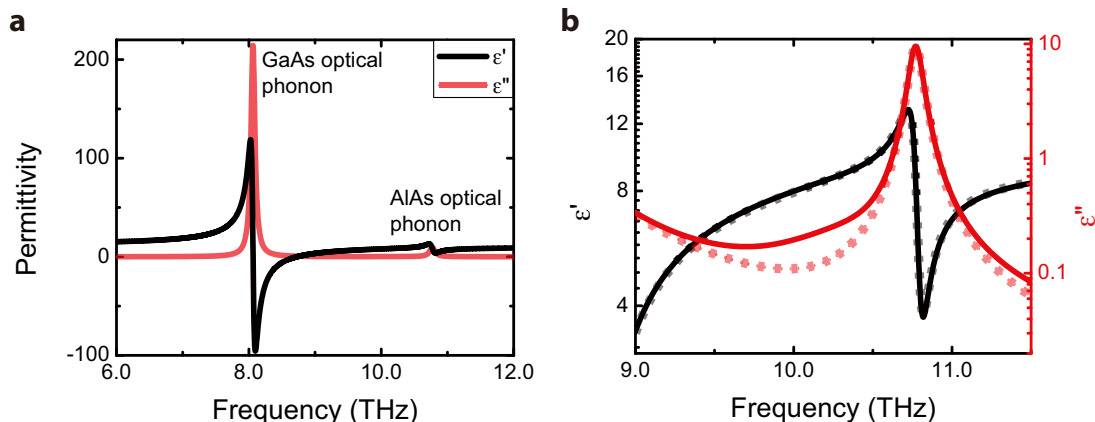
In a second step, we model the three main ISTs as anisotropic, harmonic oscillators and include their effect to the background permittivity following the intersubband selection rules. This results in an anisotropic permittivity of the form[50]:

$$\varepsilon_{QW}(\omega) = \begin{pmatrix} \varepsilon_{back}(\omega) & 0 & 0 \\ 0 & \varepsilon_{back}(\omega) & 0 \\ 0 & 0 & \varepsilon_{IST}(\omega) \end{pmatrix}, \qquad (3)$$
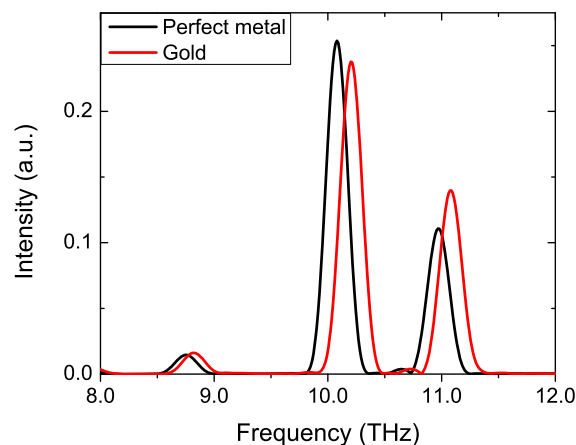
$$\varepsilon_{IST}(\omega) = \varepsilon_{back}(\omega) + \frac{N_D e^2}{\varepsilon_0 m^*}\sum_{k=2}^{4}\frac{f_{1k}}{\omega^2_{1k}-\omega^2+2i\omega\delta_{1k}}, \qquad (4)$$

where N_D describes the carrier concentration in the ground state, e the elementary charge, ε_0 the vacuum permittivity and m^* the effective electron mass. The three dominant ISTs are modelled using their oscillator strength f_{1k}, transitions frequency ω_{1k} and intersubband broadening δ_{1k}. The oscillator strengths are taken from simulations, the transition frequencies are confirmed by waveguide measurements (see next section).

It should be noted here, that the effect of the ISTs on the permittivity of the quantum-well active region is very small. We present a comparison of the modelled permittivity with and without ISTs around the dominant IST (10.4 THz) in Fig. 6b.

Figure 7 | Metamaterial resonances for a period of 4.27 µm under *Ex* excitation. The simulations using literature values for gold[51] have a spatial grid of 40 nm, the ones for a perfect metal of 200 nm. The results for a perfect metal are red-shifted by 1.2% compared to the results assuming realistic parameters for the gold contacts.
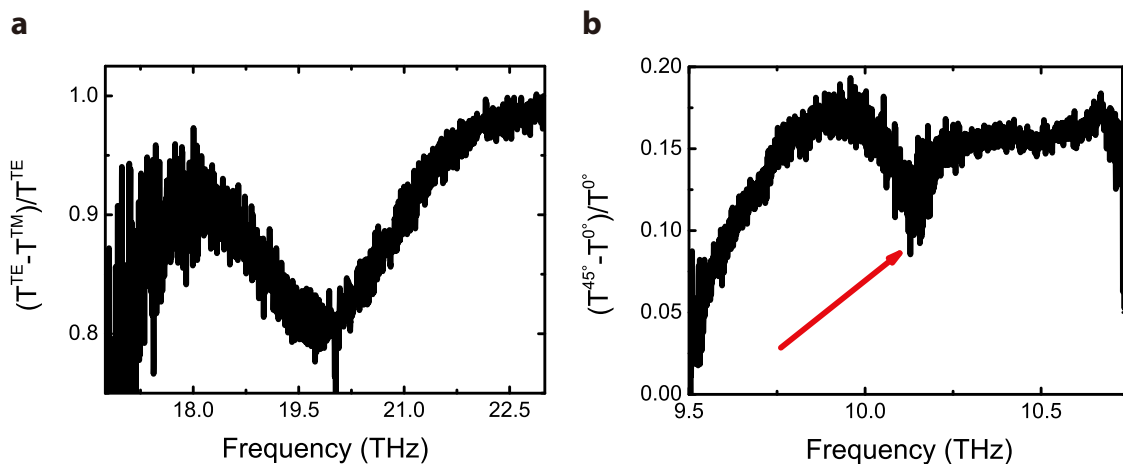
Therefore, the predicted active cavity resonances (including ISTs) show almost the same frequencies as the cold cavity resonances (without ISTs).

Realistic gold values. For all our FDTD simulations presented so far we model our gold layers as a perfect metal which allows us to reduce our simulation time significantly. One of the problems in using realistic values for the metal is the very large refractive index associated with metals. This requires an extremely fine spatial grid to fulfil the Nyquist criteria (at least two spatial sampling points per wavelength inside the medium). Perfect metal on the other hand forces a vanishing electric field at the boundary which means that there is no propagating wave inside the metal. For the simulation performed here it means that we have to increase the spatial resolution from 200 (perfect metal) to 40 nm (realistic gold). However, modelling gold as a perfect metal around the reststrahlenband creates virtually no error. We show a comparison of the metamaterial resonances for a period of 4.27 µm using perfect metal compared to literature values for gold[51] in Fig. 7. Assuming perfect metal in our simulation leads to a red-shift of the metamaterial resonances by less than 1.2% of their centre frequency.

The chosen metamaterial period of 4.27 µm is used only as an example to demonstrate the effect of realistic gold values versus a perfect metal. In order to finish the simulation within a reasonable time frame we had to reduce the size of our metamaterial unit cell. The fine spatial grid required to simulate the structure with realistic gold values made the calculation for even the smallest metamaterial period (8.54 µm) unfeasible.

Intersubband absorption measurements. To confirm the energies of our intersubband transitions we performed absorption measurements using a piece from

Figure 6 | Permittivity of THz quantum-cascade structure used for the FDTD simulations. (a), Background permittivity $\varepsilon' + i\varepsilon''$ without the effect of the intersubband transitions. The dispersion is dominated by the GaAs and the AlAs optical phonons. (b), Effect of the intersubband transition on the permittivity around the dominant transition (10.4 THz). The imaginary part of the permittivity (ε'') including the intersubband transitions is slightly larger (solid lines) compared to the dielectric background without the intersubband transition (dotted lines) showing the increased losses caused by the intersubband transition.

Figure 8 | Intersubband absorption measurements for unbiased quantum-wells. (a), Room temperature measurement in waveguide geometry. The absorption is centered at 19.8 THz corresponding to the $|1\rangle$–$|4\rangle$ transition. (b), Absorption measurements under 45° at 5 K. The intersubband absorption marked by the red arrow appears at 10.1 THz corresponding to the $|1\rangle$–$|3\rangle$ transition. The sharp drop in transmission below 9.8 THz is caused by the increased absorption due to optical phonons.

the same wafer that is used to fabricate our detectors. The results for the $|1\rangle$–$|4\rangle$ transition are presented in Fig. 8a. This measurement is performed at room temperature using a multi-pass waveguide geometry (both wafer facets are wedged under 45°). Only TM-polarized light provides an electric field component that is parallel to the growth direction of the semiconductor heterostructure and can therefore be coupled to IST. The transition is centred at 19.8 THz which agrees well with our bandstructure calculation.

To capture the $|1\rangle$–$|3\rangle$ transition we compare the change in single-pass transmission between light that illuminates the wafer under normal incidence and under 45° (Fig. 8b). Tilting the wafer provides the necessary TM polarization that allows to couple to the IST. A clear absorption peak appears at 10.1 THz which agrees well with the predicted position of the $|1\rangle$–$|3\rangle$ transition. The very strong absorption in the reststrahlenband prevents us from measuring the intersubband absorption in multi-pass waveguide geometry.

Fabrication. The metamaterial detector fabrication follows the same basic steps as the fabrication of THz quantum-cascade lasers in double-metal waveguides[25]. Our quantum-cascade structure is grown by molecular beam epitaxy on top of a semi-insulating GaAs wafer. The wafer is cleaved into multiple 1×1 cm^2 pieces for easier handling. We evaporate Ge/Au/Ni/Au (15/30/14/200 nm), which will allow for ohmic contacts in a later fabrication stage, onto the individual small pieces covering the entire epi-layer. The quantum-well stack is flipped upside down and wafer-bonded onto a doped receptor substrate that is covered with Ti/Au (10/750 nm). We use a commercial thermo-compression bonding system (EVG 501); 700 N and 320°C are applied for 30 min resulting in a mechanically robust contact. The semi-insulating GaAs wafer (used as the growth template for the quantum-cascade structure) is removed in two steps. First, the wafer is thinned to 50 μm by mechanical lapping. Second, the GaAs is etched selectively using $NH_4OH : H_2O_2 = 1 : 20$. The process stops on the $Al_{.55}Ga_{.45}As$ etch-stop layer which is removed selectively using HF (38%). Now the metamaterial can be defined by optical lithography, evaporation of another Ge/Au/Ni/Au contact and subsequent lift-off. The detector mesas are structured by optical lithography and etched using $H_2SO_4 : H_2O_2 : H_2O = 1 : 8 : 2$. A 500 nm thick SiN_x layer is deposited on the entire sample using plasma-enhanced chemical vapour deposition. The excess insulator is removed using reactive-ion etching and SF_6. The extended contacts are defined by optical lithography and sputtered using argon-plasma (Ti/Au: 10/300 nm). In a last step, the entire sample is annealed for 60 s at 420°C in a H_2N_2 (10% H_2) forming gas environment to achieve ohmic contacts. The final devices are mounted on a copper heatsink using indium and wire bonded for electrical contacts.

Detector measurements. For the spectral measurements we use a Bruker Vertex80 Fourier transform infrared spectrometer. The signal from the internal globar is guided through the Michelson interferometer and then focused onto our metamaterial detector. We use a Mylar multilayer beamsplitter covering the frequency range from 1 to 20 THz at once. A polarizer is placed directly in front of the cryostat window to set the correct excitation polarization. The photovoltage response of the metamaterial detector is fed into an analogue voltage amplifier and used as the detector signal for the spectrometer. The entire beam path is purged with dry air to reduce the atmospheric absorptions.

In contrast to our NEGF simulations where we have calculated the photocurrent, in the experiment we measure the photovoltage. We would like to point out here that both quantities give the same qualitative photoresponse. In a simple pn-junction operated in photovoltaic mode the photocurrent is created by carrier being separated and moved by the built-in field. The photovoltage (often called open-circuit voltage)

is caused by different chemical potential between the positive and negative charges being separated[52]. Nevertheless, there is a direct relation between the two quantities[53,54]. In our case, we do not have a pn-junction which creates a built-in field but we use a quantum-cascade structure that moves carriers preferably towards one direction resulting in the same qualitative behaviour. We chose to measure the photovoltage since it results in a higher signal to noise ratio compared to the photocurrent.

1. Pendry, J. B. Negative refraction makes a perfect lens. *Phys. Rev. Lett.* **85**, 3966–3969 (2000).
2. Fang, N., Lee, H., Sun, C. & Zhang, X. Sub-diffraction-limited optical imaging with a silver superlens. *Science* **308**, 534–537 (2005).
3. Veselago, V. G. The electrodynamics of substances with simultaneously negative values of e and m. *Sov. Phys. Usp.* **10**, 509 (1968).
4. Shelby, R. A., Smith, D. R. & Schultz, S. Experimental verification of a negative index of refraction. *Science* **292**, 77–79 (2001).
5. Schurig, D. *et al.* Metamaterial electromagnetic cloak at microwave frequencies. *Science* **314**, 977–980 (2006).
6. Ni, X., Ishii, S., Kildishev, A. V. & Shalaev, V. M. Ultra-thin, planar, Babinet-inverted plasmonic metalenses. *Light: Science & Applications* **2**, e72–e72 (2013).
7. Kildishev, A. V., Boltasseva, A. & Shalaev, V. M. Planar Photonics with Metasurfaces. *Science* **339**, 1232009–1232009 (2013).
8. Yu, N. *et al.* Light Propagation with Phase Discontinuities: Generalized Laws of Reflection and Refraction. *Science* **334**, 333–337 (2012).
9. O'Hara, J. F. *et al.* Thin-film sensing with planar terahertz metamaterials: sensitivity and limitations. *Opt. Express* **16**, 1786–1795 (2008).
10. Chen, H.-T. *et al.* A metamaterial solid-state terahertz phase modulator. *Nat. Phot.* **3**, 148–151 (2009).
11. Grady, N. K. *et al.* Terahertz Metamaterials for Linear Polarization Conversion and Anomalous Refraction. *Science* **340**, 1304–1307 (2013).
12. Benz, A. *et al.* Strong coupling in the sub-wavelength limit using metamaterial nanocavities. *Nat. Commun.* **4**, 2882–2882 (2013).
13. Zhang, S. Y. *et al.* λ ≈ 3.1 μm room temperature InGaAs/AlAsSb/InP quantum cascade lasers. *Appl. Phys. Lett.* **90**, 031106–031106 (2009).
14. Walther, C. *et al.* Quantum cascade lasers operating from 1.2 to 1.6 THz. *Appl. Phys. Lett.* **91**, 131122–131122 (2007).
15. Wang, X. *et al.* Ultra-sensitive mid-infrared evanescent field sensors combining thin-film strip waveguides with quantum cascade lasers. *Analyst*, 10.1039/C1031AN15787F (2012).
16. Benz, A. *et al.* Terahertz active photonic crystals for condensed gas sensing. *Sensors* **11**, 6003–6014 (2011).
17. Levine, B. F. Quantum-well infrared photodetectors. *J. Appl. Phys.* **74**, R1–R81 (1993).
18. Tidrow, M. Z., Choi, K. K., DeAnni, A. J., Chang, W. H. & Svensson, S. P. Grating coupled multicolor quantum well infrared photodetectors. *Appl. Phys. Lett.* **67**, 1800–1802 (1995).
19. Lundqvist, L., Andersson, J. Y., Paska, Z. F., Borglind, J. & Haga, D. Efficiency of grating coupled AlGaAs/GaAs quantum well infrared detectors. *Appl. Phys. Lett.* **63**, 3361–3363 (1993).
20. Kalchmair, S. *et al.* Photonic crystal slab quantum well infrared photodetector. *Appl. Phys. Lett.* **98**, 011105–011105 (2011).
21. Grant, P. D., Dudek, R., Buchanan, M. & Liu, H. C. Room-temperature heterodyne detection up to 110 GHz With a quantum-well infrared photodetector. *IEEE Photonics Tech. L.* **18**, 2218–2220 (2006).

22. Spuesens, T. *et al.* Compact Integration of Optical Sources and Detectors on SOI for Optical Interconnects Fabricated in a 200 mm CMOS Pilot Line. *J. Lightwave Tech.* **30**, 1764–1770 (2012).

23. Müller, P., Kopp, D., Llobera, A. & Zappe, H. Optofluidic router based on tunable liquid–liquid mirrors. *Royal Society of Chemistry* **14**, 737–743 (2014).

24. Levi, O., Lee, T. T., Lee, M. M., Smith, S. J. & Harris, J. S. Integrated semiconductor optical sensors for cellular and neural imaging. *Appl. Opt.* **46**, 1881–1889 (2007).

25. Kohen, S., Williams, B. S. & Hu, Q. Electromagnetic modeling of terahertz quantum cascade laser waveguides and resonators. *J. Appl. Phys.* **97**, 053106–053106 (2005).

26. Scalari, G. *et al.* Ultrastrong coupling of the cyclotron transition of a 2D electron gas to a THz metamaterial. *Science* **335**, 1323–1326 (2012).

27. Geiser, M. *et al.* Strong light-matter coupling at terahertz frequencies at room temperature in electronic LC resonators. *Appl. Phys. Lett.* **97**, 191107–191107 (2010).

28. Dietze, D., Benz, A., Strasser, G., Unterrainer, K. & Darmo, J. Terahertz meta-atoms coupled to a quantum well intersubband transition. *Opt. Express* **19**, 13700–13706 (2011).

29. Albo, A., Fekete, D. & Bahir, G. Photocurrent spectroscopy of intersubband transitions in GaInAsN/(Al)GaAs asymmetric quantum well infrared photodetectors. *J. Appl. Phys.* **112**, 084502–084502 (2012).

30. Choi, K. K. *et al.* Resonator-quantum well infrared photodetectors. *Appl. Phys. Lett.* **103**, 201113–201113 (2013).

31. Ravikumar, A. P. *et al.* Room temperature and high responsivity short wavelength II–VI quantum well infrared photodetector. *Appl. Phys. Lett.* **102**, 161107–161107 (2013).

32. Zhai, S.-Q., Liu, J.-Q., Liu, F.-Q. & Wang, Z.-G. A normal incident quantum cascade detector enhanced by surface plasmons. *Appl. Phys. Lett.* **100**, 181104–181104 (2012).

33. Sakr, S. *et al.* Two-color GaN/AlGaN quantum cascade detector at short infrared wavelengths of 1 and 1.7 μm. *Appl. Phys. Lett.* **100**, 181103–181103 (2012).

34. Barve, A. V. & Krishna, S. Photovoltaic quantum dot quantum cascade infrared photodetector. *Appl. Phys. Lett.* **100**, 021105–021105 (2012).

35. Zhai, S.-Q. *et al.* 19 μm quantum cascade infrared photodetectors. *Appl. Phys. Lett.* **102**, 191120–191120 (2013).

36. Sakr, S. *et al.* GaN/AlGaN waveguide quantum cascade photodetectors at λ ≈ 1.55 μm with enhanced responsivity and 40 GHz frequency bandwidth. *Appl. Phys. Lett.* **102**, 011135–011135 (2013).

37. Williams, B. S., Callebaut, H., Kumar, S., Hu, Q. & Reno, J. L. 3.4-THz quantum cascade laser based on longitudinal-optical-phonon scattering for depopulation. *Appl. Phys. Lett.* **82**, 1015–1017 (2002).

38. Benz, A. *et al.* The influence of doping on the performance of terahertz quantum-cascade lasers. *Appl. Phys. Lett.* **90**, 101107–101107 (2007).

39. Datta, S. *Quantum transport: Atom to transistor.* (Cambridge University Press, Cambridge, 2005).

40. Henrickson, L. E. Nonequilibrium photocurrent modeling in resonant tunneling photodetectors. *J. Appl. Phys.* **91**, 6273–6281 (2002).

41. Lake, R., Klimeck, G., Bowen, R. C. & Jovanovic, D. Single and multiband modeling of quantum electron transport through layered semiconductor devices. *J. Appl. Phys.* **81**, 7845–7869 (1997).

42. Anantram, M. P., Lundstrom, M. S. & Nikonov, D. E. Modeling of Nanoscale Devices. *Proceedings of the IEEE* **96**, 1511–1550 (2008).

43. Kubis, T., Yeh, C. & Vogl, P. Quantum theory of transport and optical gain in quantum cascade lasers. *phys. stat. sol. (c)* **5**, 232–235 (2008).

44. Krall, M., Benz, A., Schwarz, S. & Unterrainer, K. Non-equilibrium Green's function simulations on photocurrent. in preparation.

45. Falcone, F. *et al.* Babinet principle applied to the design of metasurfaces and metamaterials. *Phys. Rev. Lett.* **93**, 197401–197401 (2004).

46. Oskooi, A. F. *et al.* MEEP: A flexible free-software package for electromagnetic simulations by the FDTD method. *Comput. Phys. Commun.* **181**, 687–702 (2010).

47. Ordal, M. A. *et al.* Optical properties of the metals Al, Co, Cu, Au, Fe, Pb, Ni, Pd, Pt, Ag, Ti, and W in the infrared and far infrared. *Appl. Opt.* **22**, 1099–1120 (1983).

48. Adachi, S. *Handbook on the physical properties of semiconductors.* Vol. 2 (Kluwer Academic Publisher, 2004).

49. Chassagneux, Y. *et al.* Electrically pumped photonic-crystal terahertz lasers controlled by boundary conditions. *Nature (London)* **457**, 174–178 (2009).

50. Gabbay, A. & Brener, I. Theory and modeling of electrically tunable metamaterial devices using inter-subband transitions in semiconductor quantum wells. *Opt. Express* **20**, 6584–6597 (2012).

51. Holm, R. T., Gibson, J. W. & Palik, E. D. Infrared reflectance studies of bulk and epitaxial-film n-type GaAs. *J. Appl. Phys.* **48**, 212–223 (1977).

52. Heyszenau, H. Electron transport in the bulk photovoltaic effect. *Phys. Rev. B* **18**, 1586–1592 (1978).

53. Sinton, R. A. & Cuevas, A. Contactless determination of current–voltage characteristics and minority-carrier lifetimes in semiconductors from quasi-steady-state photoconductance data. *Appl. Phys. Lett.* **69**, 2510–2512 (1996).

54. Zhang, J. *et al.* Enlarging photovoltaic effect: combination of classic photoelectric and ferroelectric photovoltaic effects. *Sci. Rep.* **3**, 1–6 (2013).

Acknowledgments

Author contributions

A.B. performed the FTIR measurements and wrote the manuscript; M.K. performed the non-equilibrium Green's function analysis; S.S. optimised the metamaterial and fabricated the devices; D.D. designed the metamaterial; H.D. and A.M.A. grew the semiconductor wafer; W.S., G.S. and K.U. supervised the analysis and edited the manuscript. All authors discussed the results and implications and commented on the manuscript at all stages.

Additional information